nature electronics

Supplementary information https://doi.org/10.1038/s41928-026-01714-0

A wearable-to-implant wireless power transfer technology with variation tolerance

In the format provided by the authors and unedited

Table of Contents

Supplementary Note 1 | Performance benchmarking of wireless power transfer strategies for implantable bioelectronics.

A variety of wireless power transfer (WPT) modalities have been explored to support battery-free soft bioelectronics. However, selecting an optimal strategy requires balancing conflicting performance metrics: efficiency, operating depth, miniaturization, and alignment tolerance (Supplementary Table 1).

Capacitive coupling utilizes electric fields to transfer energy and can achieve high efficiency at sub-millimeter proximity. Due to its short range, this method is primarily deployed in superficial skin-interfaced biosensors or epidermal electronics. However, its utility is severely restricted by the rapid decay of electric fields over distance. Consequently, performance degrades precipitously even with slight misalignment (<1 mm tolerance), rendering it unsuitable for deep tissue implants that require stable power delivery through skin and bone.

Near-field inductive coupling (NIC) represents the clinical gold standard, widely employed in cochlear implants and rechargeable DBS systems. Although highly efficient at shallow depths, standard NIC systems depend heavily on precise alignment between rigid coils. Without active tuning employed, their transfer efficiency drops significantly with a few centimeters of displacement, and the lack of alignment tolerance leads to system failure under lateral misalignment (~5 mm) or mechanical strain, limiting their use in dynamic physiological environments.

Magnetoelectric transduction exploits the low attenuation of magnetic fields to reach deeper tissues (>50 mm). While this offers a theoretical advantage in depth, the overall end-to-end efficiency remains low (typically <10%). Furthermore, the magnetostrictive mechanism exhibits strong anisotropy; thus, power transfer is highly susceptible to angular misalignment (angle-sensitive), which undermines reliability in freely moving organs where the relative orientation of the device constantly changes. Additionally, long-term safety data in humans are still limited, keeping this approach largely in the preclinical stage.

Ultrasound-based WPT offers an alternative for deep-tissue powering (>50 mm) via acoustic focusing. Nevertheless, they face fundamental hurdles, including low electromechanical conversion efficiency and the necessity for acoustic coupling media (*e.g.*, gels) to minimize reflection. Moreover, the inherent rigidity of high-power piezoelectric ceramic transducers restricts their integration into soft, conformal bioelectronic platforms.

Mid-field electromagnetic transfer utilizes patterned transmitters to focus energy deep into biological tissues (>50 mm) by manipulating interference patterns. This approach enables significant miniaturization of implants to the millimeter scale. However, the end-to-end efficiency is constrained due to substantial tissue absorption at gigahertz frequencies. Furthermore, relying on constructive interference requires precise phase matching; thus, the focal point can be easily disrupted by tissue deformation or motion, making consistent powering challenging in dynamic cardiac or gastric environments compared to lower-frequency magnetic coupling.

In contrast to these conventional trade-offs, **the PT-symmetric resonance with strain-insensitive liquid metal technologies introduced in this work** provides a comprehensive solution for battery-free soft bioelectronics. Unlike standard NIC systems that operate at fixed frequencies, our system employs an active PT-symmetric feedback loop that automatically compensates for the detuning caused by misalignment and deformation. This capability enables the system to maintain stable high tranfer efficiency (>60%) at clinically relevant depths (40 mm) even under severe operating conditions, including 30 mm lateral misalignment and 30% mechanical strain, thereby overcoming the limitations of existing rigid or low-efficiency WPT modalities. The primary limitation of this approach is miniaturization; while liquid metal coils offer superior deformability, reducing the implant footprint to millimeter scale—as achieved by mid-field or magnetoelectric receivers—remains challenging due to fundamental physical constraints. In particular, with the current material conductivity and system power requirements, further scaling down the coil size inevitably results in reduced transfer efficiency (see details in Supplementary Notes 5 and 9).

In summary, existing WPT modalities face inherent trade-offs between efficiency, depth, alignment tolerance, and mechanical compliance. Conventional capacitive and inductive schemes excel in static, superficial applications but falter in dynamic physiological environments. Magnetoelectric, acoustic, or mid-field methods extend the operating range yet remain constrained by low end-to-end efficiency, focusing instability, or a lack of clinical maturity. The proposed system in this work bridges these gaps. It inherits the clinically proven biosafety of inductive coupling while uniquely achieving what conventional systems cannot: maintaining high efficiency under severe misalignment and deformation. This positions it as a practical platform for the next generation of reliable soft bioelectronic therapeutics.

Supplementary Note 2 | Parity-Time (PT) symmetric wireless power transfer system.

The concept of PT symmetry, originating from non-Hermitian quantum mechanics, has found compelling applications in various physical systems, including wireless power transfer. A PT-symmetric wireless power transfer system consists of two coupled resonators: a source (transmitter) resonator incorporating a gain element and a receiver resonator with inherent loss (*e.g.*, from the load and intrinsic coil resistance).

According to the coupled-mode theory, the dynamics of such a coupled-resonator system can be described by a Hamiltonian, H; $\frac{d}{dt}\begin{pmatrix} a_S \\ a_R \end{pmatrix} = H\begin{pmatrix} a_S \\ a_R \end{pmatrix}$, where a_S and a_R are the field amplitudes of the source and the receiver, which are associated with the voltage of each resonator as $a_{S,R} = \sqrt{C_{S,R}/2}V_{S,R}$. When we denote the source resonator's resonant frequency as ω_S and the nonlinear, saturable gain rate as g_S, the receiver resonator's resonant frequency as ω_R and the loss rate as γ_R, coupling rate as $\kappa = \omega k/2$ where k is the coupling coefficient between coils, the Hamiltonian can be expressed as follows[1]:

$$H = \begin{pmatrix} i\omega_S + g_S & -i\kappa \\ -i\kappa & i\omega_R - \gamma_R \end{pmatrix}. \tag{S1}$$

A system is defined as PT symmetric if its Hamiltonian H remains invariant under combined operations of parity (P) and time-reversal (T), satisfying the condition $PTH = HPT$. When the source and receiver resonators have an identical resonant frequency $\omega_S = \omega_R$, the PT symmetry is established when the gain of the source balances the loss of the receiver ($g_S = \gamma_R$)

The eigenvalues of this Hamiltonian, which correspond to the eigenfrequencies (ω) of the coupled system, are found by solving the characteristic equation $\det(H - i\omega I) = 0$, where I is the identity matrix. This yields

$$\big(\omega - (\omega_S - ig_S)\big)\big(\omega - (\omega_R + i\gamma_R)\big) - \kappa^2 = 0. \tag{S2}$$

At a steady state, the system oscillates at one of its real eigenfrequencies ω. To calculate ω, one can separate the real and imaginary parts of the equation (S2) and obtain

$$(\omega - \omega_S)(\omega - \omega_R)^2 + \gamma_R^2(\omega - \omega_S) - \kappa^2(\omega - \omega_R) = 0 \quad \text{(S3)}$$

$$g_{S,sat}(\omega - \omega_R) = \gamma_R(\omega - \omega_S) \quad \text{(S4)}$$

The equation (S3) is a third-order polynomial, which implies it has one to three real solutions forming a steady-state frequency surface depending on system parameter values $\Delta\omega/\omega_S = (\omega_R - \omega_S)/\omega_S$ and κ/γ_R (Supplementary Fig. 12a). The topology of this surface reveals the stability characteristics of the system; the red regions represent stable states that the system naturally selects for steady-state oscillation, while the blue regions denote unstable states that are physically inaccessible[2]. The followings are noteworthy from the topology of the steady-state frequency surface.

1. **When the resonators are matched (ω_S=ω_R=ω_0) :** This corresponds to the cross section of the steay-state frequency surface with the plane $\Delta\omega/\omega_s = 0$ (indicated by the solid red line in Supplementary Fig. 12a). The system exhibits two distinct phases depending on the relationship between the coupling coefficient κ and the loss rate γ_R:

   A. **Unbroken PT-symmetric phase ($\kappa > \gamma_R$):** In this strong coupling regime, the system reaches a steady state in which the oscillating frequency ω is not ω_0, but one of two stable real eigenfrequencies $\omega = \omega_0 \pm \sqrt{(\kappa^2 - \gamma_R^2)}$. The system oscillates at one of these eigenfrequencies, typically the one requiring a lower saturated gain. This self-selection mechanism allows the system to adapt its operating frequency to maintain resonance despite changes in κ caused by variations in distance, alignment, or deformation. Moreover, the condition $g_{S,sat} = \gamma_R$ from (S4) ensures the system remains in the unbroken PT-symmetric regime. In this phase, the receiver and source maintain equal voltage amplitude (V_R=V_S), thereby enabling robust power transfer.

B. **Broken PT-symmetric phase (κ < γ_R):** In this weak coupling regime, the system possesses a single real eigenfrequency ω_0 at which the system oscillates. This implies that the presence of the weakly-coupled receiver does not affect the oscillation frequency of the source. Since the system oscillates at source's self-resonant frequency ($\omega = \omega_0$), the nonlinear saturated gain $g_{S,sat}$ fails to balance the loss rate γ_R, regardless of Eq. (S4). This imbalance ($g_{S,sat} \neq \gamma_R$) results in the broken PT symmetry, leading to the receiver's voltage amplitude lower than that of the source. Consequently, the received power becomes sensitive to variations in κ caused by environmental changes.

For a subcutaneous implantable device located a few centimeters beneath the skin, the coil can be designed sufficiently large (*e.g.*, 6 × 6 cm^2) to ensure that the coupling rate (κ) exceeds the loss rate (γ_R). This condition maintains the system within the unbroken PT-symmetric phase, providing the proposed wireless power transfer system with high robustness. Such stability against variations in receiver displacement, orientation, and rotation is experimentally validated in Fig. 3d-e, Extended Data Fig. 5d-f, and Extended Data Fig. 5g-i, respectively.

2. **When the resonators are detuned ($\omega_S \neq \omega_R$):** In case where the resonators are detuned due to mechanical deformation of the coil or medium variatons near the coil, Eq. (S4) states that the saturable gain $g_{S,sat}$ fails to precisely balance the loss rate γ_R, leading to a breakdown of PT symmetry. Nevertheless, numerial solutions of the voltage ratio $|V_R/V_S|$ based on coupled-mode theory (Supplementary Fig. 12b) show that the voltage ratio stays above 0.6 as long as the system is not severely detuned ($|\omega_R - \omega_S|/\omega_S < 0.1$). This condition corresponds to the receiver coil being stretched by less than 50% (Fig. 2j). This finding is consistent with simulation results in Supplementary Note 3 and

Supplementary Fig. 12b. This configuration enables balanced voltage distribution between the source and receiver despite coil deformation, thereby enhancing the robustness of wireless power transfer. Experimental validation of this stability under mechanical strain, as well as combined strain and displacement, is provided in Fig. 3h–i and Fig. 3j-k, respectively.

Supplementary Note 3 | Switch-mode amplifier in efficient PT-symmetric wireless power transfer.

While the theoretical framework of PT symmetry guarantees robust power transfer by maintaining resonance, the overall system efficiency also critically depends on the efficiency of the gain element itself. Early implementations of PT-symmetric WPT often utilized operational amplifier-based gain circuits[1]. While these can provide the necessary negative resistance for gain, they suffer from inherent power losses due to current flowing through resistive components within the amplifier, limiting the overall system efficiency (typically below 50% and often much lower).

To achieve high system efficiency, we employ a switch-mode amplifier (SMA), such as a Class-E amplifier, as the gain element. The primary role of the SMA is to inject power into the source resonator with minimal internal power dissipation within the amplifier itself.

The high efficiency of an SMA stems from its operational principle: the active switching device (*e.g.*, a MOSFET) alternates rapidly between a fully "on" state (low voltage drop, high current) and a fully "off" state (high voltage, near-zero current). Ideally, there is minimal overlap between the voltage across the switch and the current flowing through it. If either the voltage or the current is zero at any given time, the instantaneous power dissipated by the switch ($P = V \times I$) is also zero.

In the context of our PT-symmetric wireless power transfer system, the SMA is integrated with a current-sensing feedback loop that includes a phase delay adjustment mechanism. Through the feedback sensing the current in the source resonator (transmitter coil), a portion of energy is fed back to the gate of the SMA's switching transistor with an appropriate phase shift, enabling self-oscillation. The crucial role of the phase delay adjustment is to ensure that the gate drive signal is timed correctly relative to the oscillations in the source resonator such that the SMA operates under optimal high-efficiency switching conditions.

As established in a previous study[3], a remarkable consequence of PT symmetry in the strong coupling regime is that the effective load impedance (Z_{out}) presented to the SMA's output remains nearly constant and optimal, even as the coupling coefficient κ varies. This is because the system's self-adjustment of the oscillation frequency compensates for changes in κ, maintaining Z_{out} close to the value required for efficient SMA operation. The phase delay in the feedback loop is tuned to match the inherent phase shift between the SMA's output current and the required input gate signal for this optimal Z_{out}. Therefore, the SMA, when properly integrated into the PT-symmetric circuit with appropriate phase-delay feedback, enables the gain element to inject power into the source resonator with very high efficiency (> 90%).

Supplementary Note 4 | Impact of resonator detuning on PT-symmetric system performance.

In applications with stretchable or deformable receiver coils as used in this work, the resonant frequency of the receiver can deviate from that of the source. Mechanical deformation, such as stretching the receiver coil, primarily alters its inductance due to geometric changes, leading to a shift in its resonant frequency. This mismatch, where $\omega_S \neq \omega_R$, is known as resonator detuning and can influence the system's performance.

Our experimental characterization of the LM receiver coil, as presented in Fig. 2j, demonstrates this strain-induced frequency shift. The S_{11} measurements show that the resonant frequency of the LM coil decreases from 2.64 MHz at 0% strain to 2.39 MHz at 50% strain. Assuming ω_S is initially matched to the unstrained receiver and fixed (*e.g.*, ω_S = 2.64 MHz), a 50% strain on the receiver results in a resonant frequency ratio (ω_R/ω_S) of 2.39/2.64 ≈ 0.9.

This strain-induced detuning behavior is further analyzed in Supplementary Fig. 12, which shows simulation results of the normalized transfer efficiency $|V_R/V_S|$ as a function of the resonant frequency ratio. The region of primary interest is where the resonant frequency ratio decreases from 1.0 to 0.9, corresponding to increasing mechanical strain on the receiver. In this regime, the transfer efficiency decreases gradually from 1.09 at ω_R/ω_S = 1.0 to 0.80 at ω_R/ω_S = 0.9, representing a reduction of around 26%. The absence of any abrupt efficiency drop indicates that the system can sustain efficient energy transfer through coherent mode coupling between the source and receiver. This result demonstrates that the PT-symmetric wireless power transfer system retains functional robustness against moderate detuning, making it well-suited for deformable or stretchable electronics.

Supplementary Note 5 | Determination of the coil size for the wireless LM pacemaker.

We discuss how we determined the receiver coil size *D* of the wireless LM pacemaker to be placed at 15-mm depth. A reduction in coil size lowers the coupling rate κ with a source coil for a given transfer distance *R*, which can potentially degrade the transfer efficiency. Furthermore, the transfer distance *R* also affects the coupling rate; as *R* increases, the magnetic flux captured by the receiver coil decreases, thereby reducing κ. Based on the scale invariance of Maxwell's equations, the coupling rate is predominantly determined by the relative coil size to the transfer distance (*D/R*).

In conventional near-field inductive coupling schemes, any reduction in the coupling rate directly degrades transfer efficiency, as discussed in Fig. 3d–e. In contrast, we have demonstrated that the PT-symmetric scheme renders the transfer efficiency less dependent on κ (Fig. 3d–e). Nevertheless, if the coupling rate falls below a critical threshold, i.e., the receiver's loss rate γ_R, it is inevitable that the transfer efficiency degrades substantially as the PT symmetry breaks. Therefore, the unity-gain distance R_{unit} to achieve a near-unity transfer efficiency ($|V_R/V_S|\approx 1$) is determined by the condition that $\kappa(D/R) > \gamma_R$. Previous studies tabulated in Table R1 report that such the unity-gain distance is typically on the order of the coil diameter; $R_{\mathrm{unit}} \sim D$.

The extent to which R_{unit} can exceed D depends on the application-specific loss rate γ_R. The total loss rate of the receiver consists of the load loss γ_L and the intrinsic coil loss γ_{R0}, such that $\gamma_R = \gamma_L + \gamma_{R0}$. While coils made of thick, solid copper can achieve very low intrinsic loss—allowing R_{unit} to extend beyond the coil diameter[1,2]—this work employs a coil made of thin, liquid metal elastomer to mitigate discomfort of a patient and foreign body sensation. Because the conductivitiy of liquid metal elastomer is approximately three orders of magnitude lower than that of copper, this increases the intrinsic loss rate to be from 3.3 to 1.0 Mrad/s for the coil diameter varying from 10 to 60 mm.

The loss rate of the load γ_L also plays a critical role in determining the operational range. The receiver includes a rectifier (36 mW), a low-dropout (LDO) regulator (180 mW), and a microcontroller unit (24 mW), totaling a power consumption of 240 mW. Although the LDO regulator consumes more power than alternatives (e.g., switching regulators), it was utilized to simplify the chip footprint and ease the liquid-metal fabrication process. This power consumption of 240 mW correspondes to a load loss rate of $\gamma_L = 1.3$ Mrad/s. Consequently, the total loss rate ranges from γ_R =2.3 Mrad/s to 4.6 Mrad/s depending on the coil diameter, which constrains the unity-gain range R_{unit} to be smaller than the coil dimension D.

To investigate the effect of the receiver coil size, Supplementary Fig. 9a shows the variation of the coupling rate κ as a function of transfer distance for various receiver coil sizes (with a fixed 60 mm source coil), alongside the threshold γ_R. To maintain near-unity efficiency at the target implantation depth of 15 mm, a minimum receiver coil diameter of 60 mm is required. Diminishing the coil size further would push the coupling rate below the critical PT-symmetric threshold at the 15-mm depth, leading to a sharp efficiency degradation due to symmetry breaking.

Supplementary Note 6 | Real-time frequency adaptation and transient response.

A key characteristic of the PT-symmetric wireless power transfer system is its ability to autonomously adapt its operating frequency in real-time to maintain high transfer efficiency in response to changes in the coupling environment. To investigate the dynamics of this adaptation, we performed time-domain simulations of the system's transient response to sudden changes in the coupling coefficient (κ), mimicking abrupt movements between the transmitter and receiver.

The simulation applied step-like changes to the coupling coefficient over time, as illustrated in Supplementary Fig. 10a. It shows an initial coupling coefficient, followed by a sudden increase at t = 200 μs (*e.g.*, as distance decreases), and then a sudden decrease to a lower value at t = 250 μs (*e.g.*, as distance increases). The corresponding transfer efficiency are shown in Supplementary Fig. 10b, respectively. Upon a sudden change in κ, the system momentarily deviates from its steady-state oscillation. However, due to the inherent self-regulating nature of the nonlinear PT-symmetric system, the operating frequency and the saturated gain rapidly readjust to the new coupling condition. As a result, although the voltage amplitudes at both the source and receiver undergo a brief transient period characterized by some overshoot or undershoot, they quickly settle back to new stable steady-state amplitudes. The system quickly re-stabilized after each perturbation in the coupling factor within a few tens of microseconds (approximately 22 μs, depending on the perturbation), as indicated by the vertical black lines in Supplementary Fig. 10b. This rapid transient response, significantly faster than mechanical movements, underscores the system's suitability for dynamic wireless power transfer applications.

Supplementary Fig. 10 shows simulation results of the waveforms of the switching MOSFET. The drain-source voltage V_{DS} (blue) collapses to nearly 0 V just before the gate voltage V_{Gate} (red) turns the device on, while the drain current I_{DS} (black) decays to almost 0 A before the device is turned off. Because the two quantities cross nearly zero at their respective switching instants, the overlap between I_{DS} and V_{DS} is effectively eliminated, and the instantaneous switching power ($I_{DS} \times V_{DS}$) approaches zero. This operation minimizes switching losses and thermal stress, further supporting the high-efficiency and rapidly self-stabilizing behavior of the PT-symmetric WPT system.

Supplementary Note 7 | Efficiency of the wireless power transfer and rectification chain.

While power is delivered to the receiver in AC form, it must be converted to DC to provide a stable supply for electronic circuitry. Because the power management unit—consisting of a rectifier and a regulator—introduces its own energy losses, the overall end-to-end efficiency is lower than the power transfer efficiency defined in the Methods section. While the voltage ratio $|V_R/V_S|$ is a standard metric in the PT-symmetric WPT literature to characterize coupling robustness, we herein report the end-to-end efficiency to provide a more comprehensive and practical interpretation of the system's performance.

When the receiver includes the chain of rectifier/regulator as shown in Supplementary Fig. 13a, the end-to-end efficiency $\tilde{\eta}$ is the product of power-transfer efficiency and the efficiencies of the rectifier and the regulator:

$$\tilde{\eta} = P_{out,DC}/P_{in,AC} = \eta_{AC-AC} \cdot \eta_{AC-DC} \cdot \eta_{DC-DC}.$$

The efficiency of each stage is characterized independently. First, the power-transfer efficiency η_{AC-AC} was derived from the measured peak-to-peak voltages of the transmitter and the receiver, as detailed in the Methods. The rectifier was implemented as a voltage-doubler variant, with specific capacitance values and the diode models provided in Supplementary Fig. 13b. To evaluate the efficiency of the rectifier, we terminated the rectifier with a 550-Ω load resistance, representing the equivalent impedance of the receiver electronics (MCU and stimulation). Since the efficiency η_{AC-DC} is a function of input voltage, it was obtained using Keysight ADS simulation by sweeping the input voltage from 2 to 8 V, and the resulting rectifier efficiency $\eta_{AC–DC}$ is shown in Supplementary Fig. 13d.

The rectifier is followed by a low-dropout (LDO) regulator (model: AMS1117-3.3) to ensure a stable voltage supply for the circuit. Although the efficiency of the LDO is much lower than that of switching regulator for a high input voltage, we utilized it to simplify the chip footprint and ease the LM fabrication process. The regulator efficiency η_{DC-DC} was experimentally determined by measuring the DC input/output currents and voltages while sweeping the input from 4 to 24 V (Supplementary Fig. 13c,e). As expected for an LDO architecture, the efficiency decreases with input voltage increases due to the larger voltage drop across the regulator. The resulting conversion efficiency ($\eta_{AC-DC}\times\eta_{DC-DC}$) is shown in Supplementary Fig. 13f.

Based on these conversion characteristics, we evaluated the end-to-end efficiency $\tilde{\eta}$ as a function of transfer distance. The power-transfer efficiency η_{AC-AC} between the transmitter and receiver coils is shown in Supplementary Fig. 13g. The conversion efficiency of the rectifier–regulator chain, calculated based on the input voltage at corresponding experimental distances, is depicted in Supplementary Fig. 13h. Finally, the resulting end-to-end efficiency of the system is shown in Supplementary Fig. 13i. With the input power of 0.4 W at the transmitter, the system provides a regulated output power of 24 mW, which can operate the stimulation and control electronics used in our in vivo demonstration.

Supplementary Note 8 | Discussion on safety and compatibility.

1. **Specific absorption rate (SAR):** The maximum safely deliverable power in implantable wireless systems is fundamentally constrained by tissue heating, commonly evaluated through the SAR. The SAR quantifies the rate of electromagnetic energy absorbed per unit mass of biological tissue and serves as a primary regulatory metric for RF exposure safety. According to ICNIRP guidelines, localized SAR must remain below 2 W/kg (under 10 g-averaging conditions) to prevent excessive temperature rise[4].

   Because the present system operates in the near-field inductive regime, localized SAR in tissue surrounding the implant represents the dominant safety constraint rather than far-field radiation exposure. Accordingly, electromagnetic simulations (Ansys HFSS) were performed using a layered tissue model (skin and muscle) surrounding the receiver, as illustrated in Supplementary Fig. 16a. The receiver was positioned beneath the skin layer (3 mm) and muscle layer (7 mm), representing a clinically relevant implantation depth.

   For the input power used in the in vivo animal experiment (0.4 W), the HFSS-simulated maximum averaged SAR is approximately 0.02 W/kg, as shown in Supplementary Fig. 16b. This value is nearly two orders of magnitude below the ICNIRP regulatory limit of

2 W/kg, indicating a substantial safety margin at the experimentally validated operating condition.

To evaluate power scalability, the transmitted power was increased in simulation while monitoring the peak localized SAR within the tissue domain. As shown in Supplementary Fig. 16c, SAR increases linearly with source power. Due to its nature of linearity, the SAR should reach the ICNIRP limit of 2 W/kg at approximately 38 W of input power. This indicates that the system possesses significant power scalability, with a wide margin between the demonstrated operating point (0.4 W) and the regulatory safety boundary.

2. **Electromagnetic Interference (EMI):** We investigated if the proposed system surpasses the regulation related to EMI and impose the danger of malfunction of other electronic devices by intereference.

The proposed system operates in the 1–4 MHz band. Because the coil structure of the system is much smaller than the wavelength of this frequency band, the electromagnetic field emanated from the coil is mostly reactive, and the far-field radiative emissions are inherently suppressed.

To evaluate the spectral characteristics of the self-oscillating circuit, we performed the frequency spectrum analysis of the steady-state voltage across the transmitter coil using circuit-level simulations in Supplementary Fig. 18a. The results confirm that the emission spectrum is dominated by a sharp fundamental component. Harmonic components are significantly lower in amplitude and decay rapidly, indicating minimal broadband noise or spectral spreading. This narrowband behavior inherently mitigates the risk of interference with RF systems operating at higher frequencies.

To provide an experimental reference for near-field magnetic-field emissions, we measured the magnetic field spectrum at 3-meter separation distance using a 60-cm diameter loop antenna and compared the results against the European Telecommunications Standards Institute (ETSI) EN 300 330 standards[5,6]. Since the coil structure generates a stronger magnetic energy in near field, the magnitude of the magnetic field rather than the electric field must be carefully scrutized. As shown in Supplementary Fig. 18b, the measured magnetic field in the range of 1 to 10 MHz remains well below the regulatory limit (24.5 dBμA/m, obtained from Table 2 in Clause 4.3.4 and the conversion factor in Annex H).

In conclusion, the high spectral purity of the fundamental frequency, coupled with suppressed harmonics and magnetic-field emissions that remain well within relevant compliance thresholds, collectively ensures that the potential for electromagnetic interference (EMI) is minimal under typical operating conditions.

Supplementary Note 9 | Design considerations for miniaturization of the wireless LM pacemaker.

The receiver coil size is the primary factor that determines the physical footprint of the implantable device and therefore represents the main bottleneck for device miniaturization. However, in practice, the operational distance of the system R_{max} can exceed the unity-gain transfer distance R_{unit}, providing a margin for further miniaturization. Because the source oscillation voltage (8 V) in the current configuration is significantly higher than the required voltage to operate the regulator (3.3 V), the implantable system remains functional even in the PT-broken regime. The simulation results of the available power demonstrate that the system remains operational ($P_{\mathrm{av}} > 24$ mW) up to a distance of 40 mm (black curve, Supplementary Fig.

9b), which is much longer than R_{unit} (15 mm) and consistent with the measurement results in Figs. 4f and 5f.

Another opportunity for miniaturization lies in reducing the loss rate associated with the receiver coil and the regulator. For example, improvements in the electrical conductance of the LM conductor, together with the use of more power-efficient regulators such as switching regulators, can substantially reduce the effective loss rate of the receiver. In our simulation, a tenfold increase in the electrical conductance of the LM conductor, combined with a reduction in regulator loss, decreases the intrinsic coil and regulator loss rates from 1.0 Mrad/s and 0.98 Mrad/s to 0.17 Mrad/s and 0.1 Mrad/s, respectively. As a result, the operational distance R_{max} of the 60-mm coil increases from 40 mm to 75 mm (blue curve, Supplementary Fig. 9b). By exploiting these extended performance margins, the receiver coil can be miniaturized to a 15-mm diameter while maintaining operation at the 15-mm implantation depth, provided it is equipped with the improved conductor and a switching regulator (red curve, Supplementary Fig. 9b).

In summary, given the current material conductivity and system power requirements, further miniaturization inevitably compromises transfer efficiency. Nevertheless, future advancements in the conductivity of the liquid-metal elastomer, combined with low-power system architectures such as switching regulators, hold the potential to enable further miniaturization down to approximately D = 15 mm while maintaining operation at the target depth R = 15 mm.

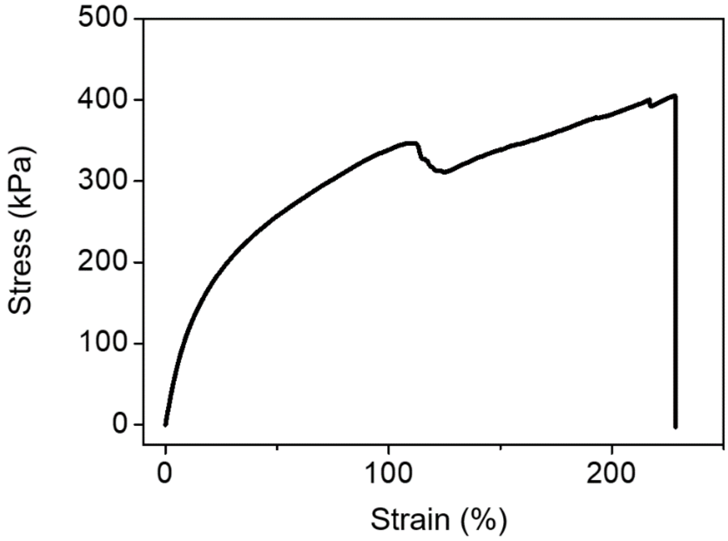

Supplementary Fig. 1 | Stress-strain curve of the wireless LM pacemaker. The device exhibits soft, elastomeric behavior with a Young's modulus of approximately 880 kPa, calculated from the initial linear region of the curve. The elongation at break is approximately 220%, demonstrating the device's high stretchability and mechanical robustness.

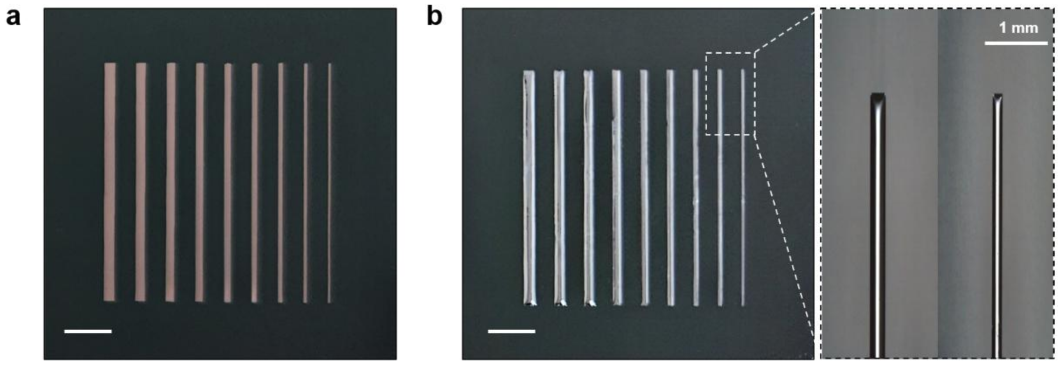

Supplementary Fig. 2 | High-resolution patterning of LM using a selective wet-coating process. Optical images of 100 nm-thick copper (Cu) lines with varying widths patterned on an SBS substrate **(a)**, and the same sample after the selective wet-coating process, where LM selectively adheres to the Cu under acidic conditions to form conductive traces **(b)**. The magnified inset demonstrates the capability to reliably form high-fidelity patterns with a minimum feature size of 200 µm. Scale bars, 5 mm (main); 1 mm (inset).

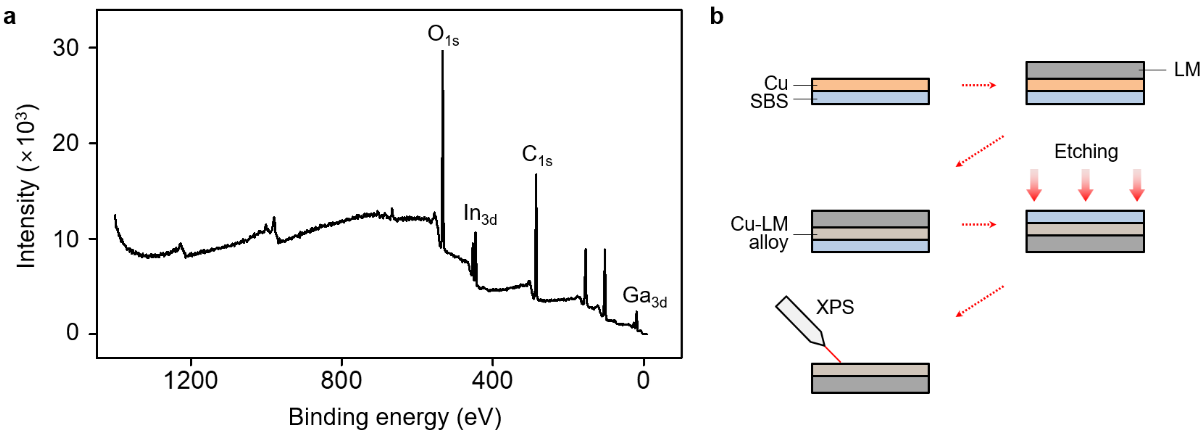

Supplementary Fig. 3 | Surface characterization of the Cu-LM interface. A, X-ray photoelectron spectroscopy (XPS) spectrum of the LM surface that was in contact with the Cu layer. The spectrum reveals prominent peaks for Gallium (Ga_{3d}) and Indium (In_{3d}), but a notable absence of a Cu signal. This absence indicates the formation of a Ga–Cu intermetallic alloy at the interface. **B**, Schematic of the sample preparation for XPS analysis. A Cu-coated SBS substrate was coated with LM, and the SBS was subsequently removed by reactive ion etching (RIE) to expose the bottom Cu-LM interface for characterization.

Supplementary Fig. 4 | Robust integration of commercial chip components under strain. An optical image demonstrating the reliable integration of commercial chips with the LM interconnects while subjected to 50% uniaxial strain. The stable mechanical and electrical connection is maintained even at this level of deformation, creating stretchable electronic systems. Scale bars, 1 mm.

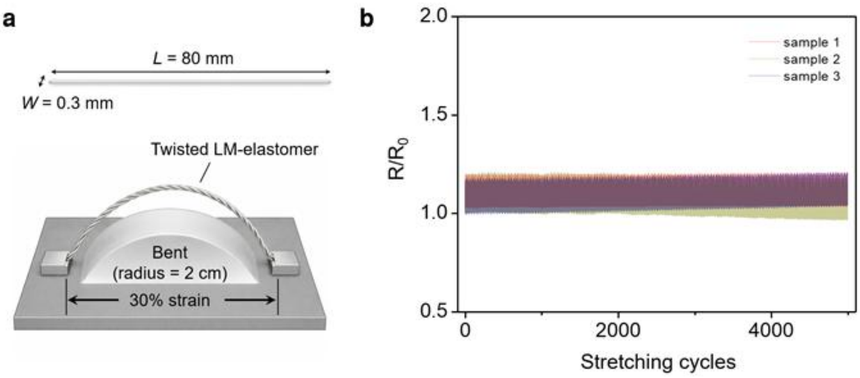

Supplementary Fig. 5 | Mechanical fatigue stability of the LM–elastomer conductor under combined deformation. a, Schematic illustration of the LM-elastomer conductor subjected to simultaneous stretching (30% strain), bending (radius = 2 cm), and twisting (3 turns). **b**, Normalized resistance change during 5,000 stretching cycles under combined deformation (n = 3 samples).

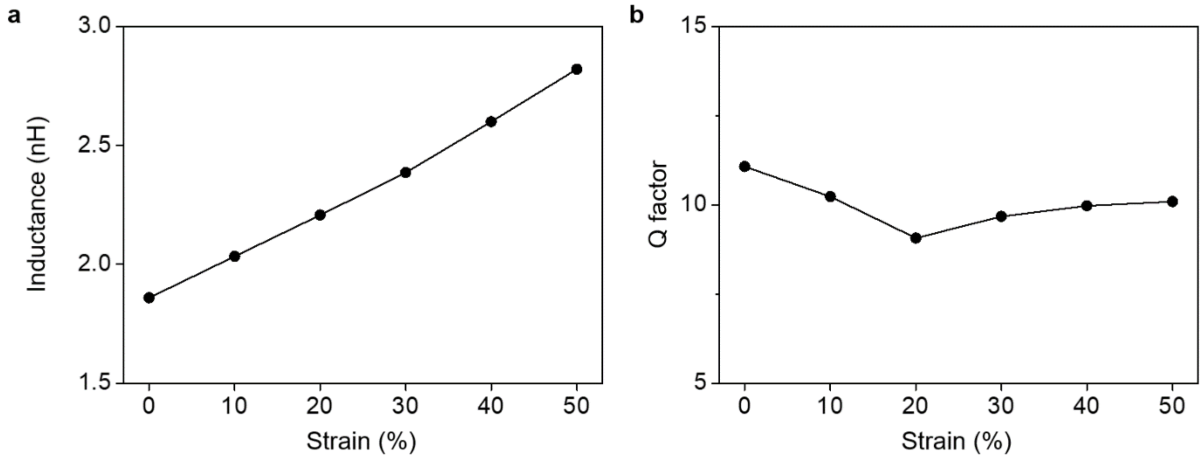

Supplementary Fig. 6 | RF characteristics of the LM device under strain. Simulation results of coil inductance **(a)** and Q factor **(b)** of the LM receiver under uniaxial strain up to 50%. The inductance increases with strain, reflecting geometric changes during stretching.

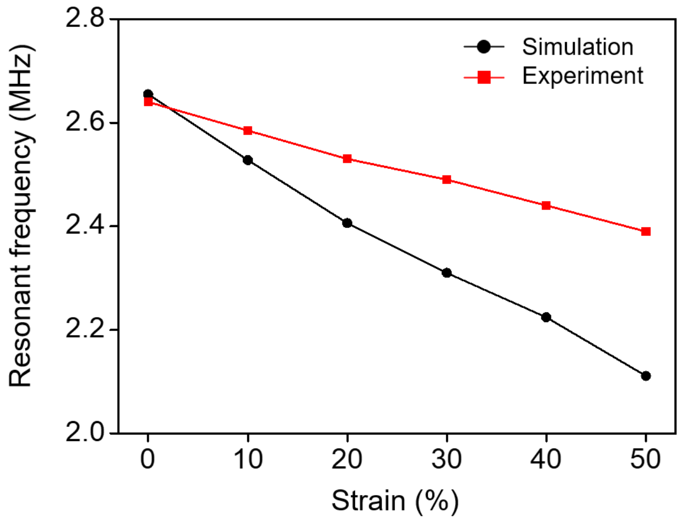

Supplementary Fig. 7 | Resonant frequency of the LM coil under strain. Comparison of simulated (black) and measured (red) self-resonant frequency of the LM coil as a function of applied strain. The resonant frequency decreases with increasing strain in both simulation and experiment. This trend is consistent with the observed increase in coil inductance (as shown in Supplementary Fig. 5a), which is the dominant factor influencing the resonant frequency.

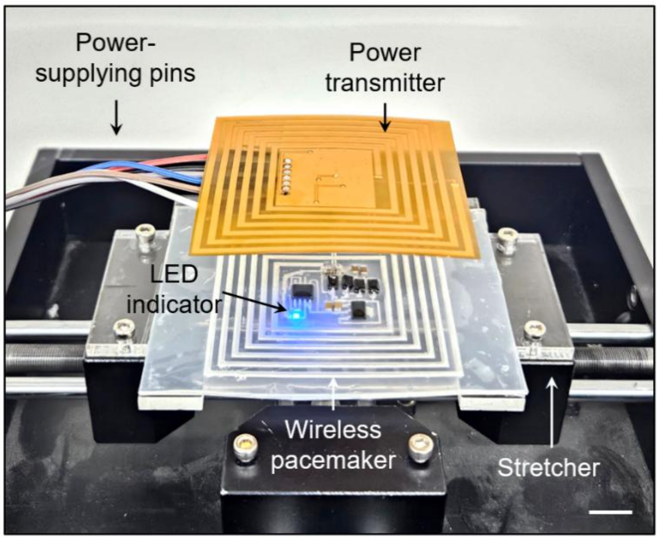

Supplementary Fig. 8 | Experimental setup for characterizing the wireless power transfer system. An optical image of the testing platform used to evaluate the performance of the wireless power transfer system under controlled mechanical strain. The platform consists of a flexible power transmitter, a wireless LM pacemaker (receiver) with an LED indicator, and a motorized stretcher for applying precise uniaxial strain. The LED provides a visual confirmation of successful power transmission to the receiver. Scale bar, 1 cm.

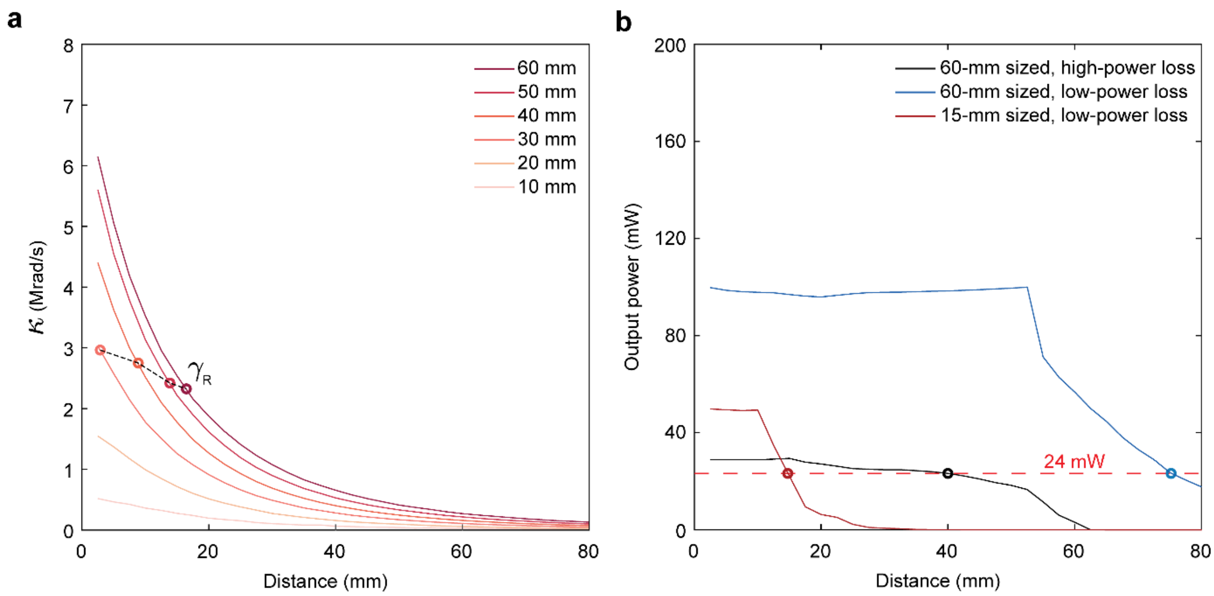

Supplementary Fig. 9 | Effect of receiver coil size on coupling rate and transfer efficiency. **a,** Simulated coupling rate (κ) as a function of transfer distance for receiver coils with diameters ranging from 10 to 60 mm, while keeping the transmitter coil diameter fixed at 60 mm. The markers denote the receiver loss rate (γ_R) for each coil size. **b,** Corresponding simulated transfer efficiency $|V_R/V_S|$ as a function of transfer distance for different receiver coil diameters.

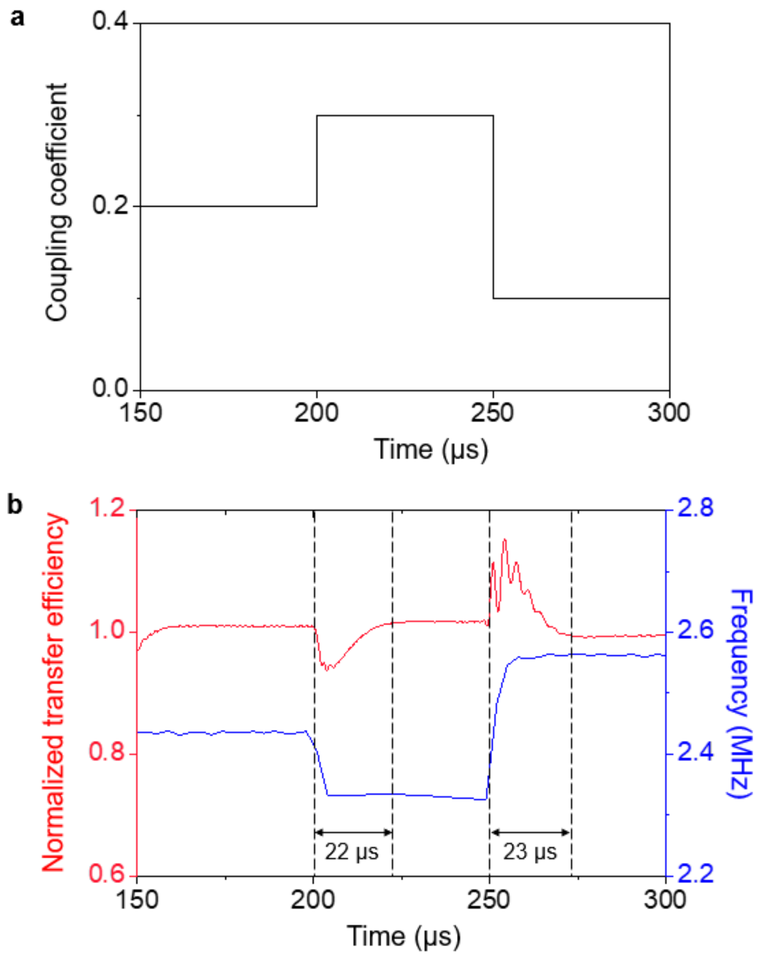

Supplementary Fig. 10 | Real-time adaptive response of the PT-symmetric system. A, Simulated step-wise changes in the coupling coefficient over time, mimicking abrupt changes in distance or alignment between the transmitter and receiver. **B**, The corresponding real-time adaptation of the system's operating frequency (blue line) and normalized transfer efficiency (red line). The system demonstrates rapid self-stabilization, reaching a new steady state within approximately 22–23 μs after each perturbation.

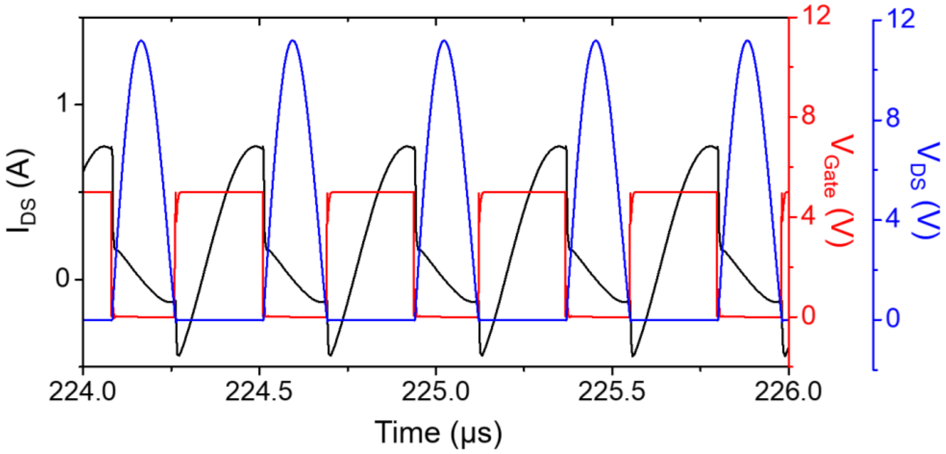

Supplementary Fig. 11 | Simulated switching waveforms of the MOSFET. Waveforms of the drain-source voltage (V_{DS}, blue), gate voltage (V_{Gate}, red), and drain current (I_{DS}, black) in the transmitter. V_{DS} drops to nearly zero before I_{DS} rises, and I_{DS} falls to zero before V_{DS} rises. This minimizes the overlap between voltage and current, thereby significantly reducing switching losses and contributing to the system's high overall efficiency.

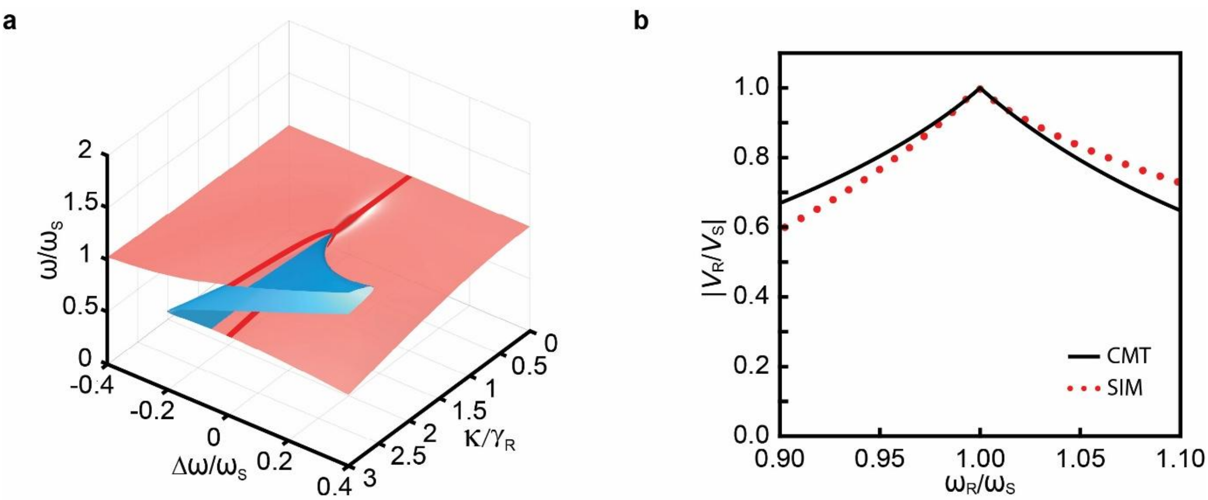

Supplementary Fig. 12 | Steady-state frequency and efficiency for variations in system parameters. a, Steady-stae frequency surface as a function of frequency detuning ($\Delta\omega/\omega_S$) and the coupling-to-loss ratio (κ/γ_R). **b,** Simulated transfer efficiency ($|V_R/V_S|$) as a function of the ratio between the receiver's (ω_R) and the source's (ω_S) resonant frequencies. This illustrates the system's robustness against frequency detuning, which can be induced by mechanical strain, and confirms the system's ability to tolerate moderate strain-induced frequency shifts.

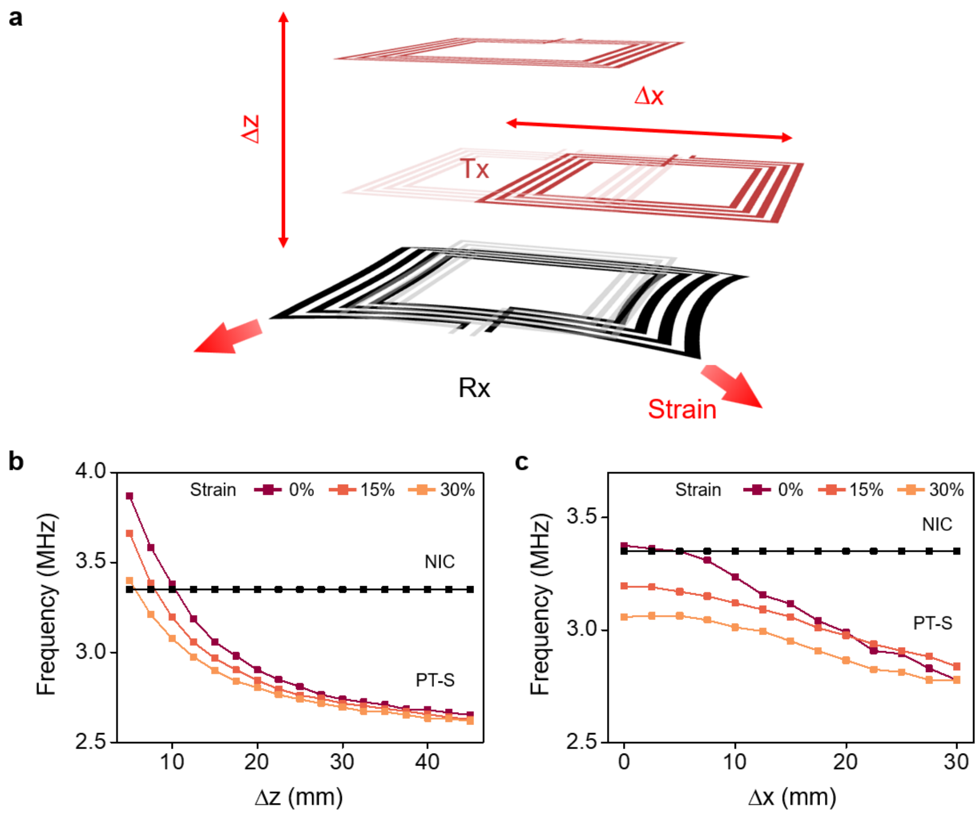

Supplementary Fig. 13 | Frequency response to simultaneous geometric and mechanical variations. a, Schematic illustration of variations: axial separation (Δz), lateral misalignment (Δx), and mechanical strain applied to the receiver (Rx). **b**, **c**, Measured operating frequency of the PT-symmetric (PT-S) system and the conventional near-field inductive coupling (NIC) system as a function of Δz **(b)** and Δx **(c)** at different strain levels (0%, 15%, 30%). The PT-S system dynamically adjusts its frequency to adapt to changes in both geometric positioning and mechanical strain.

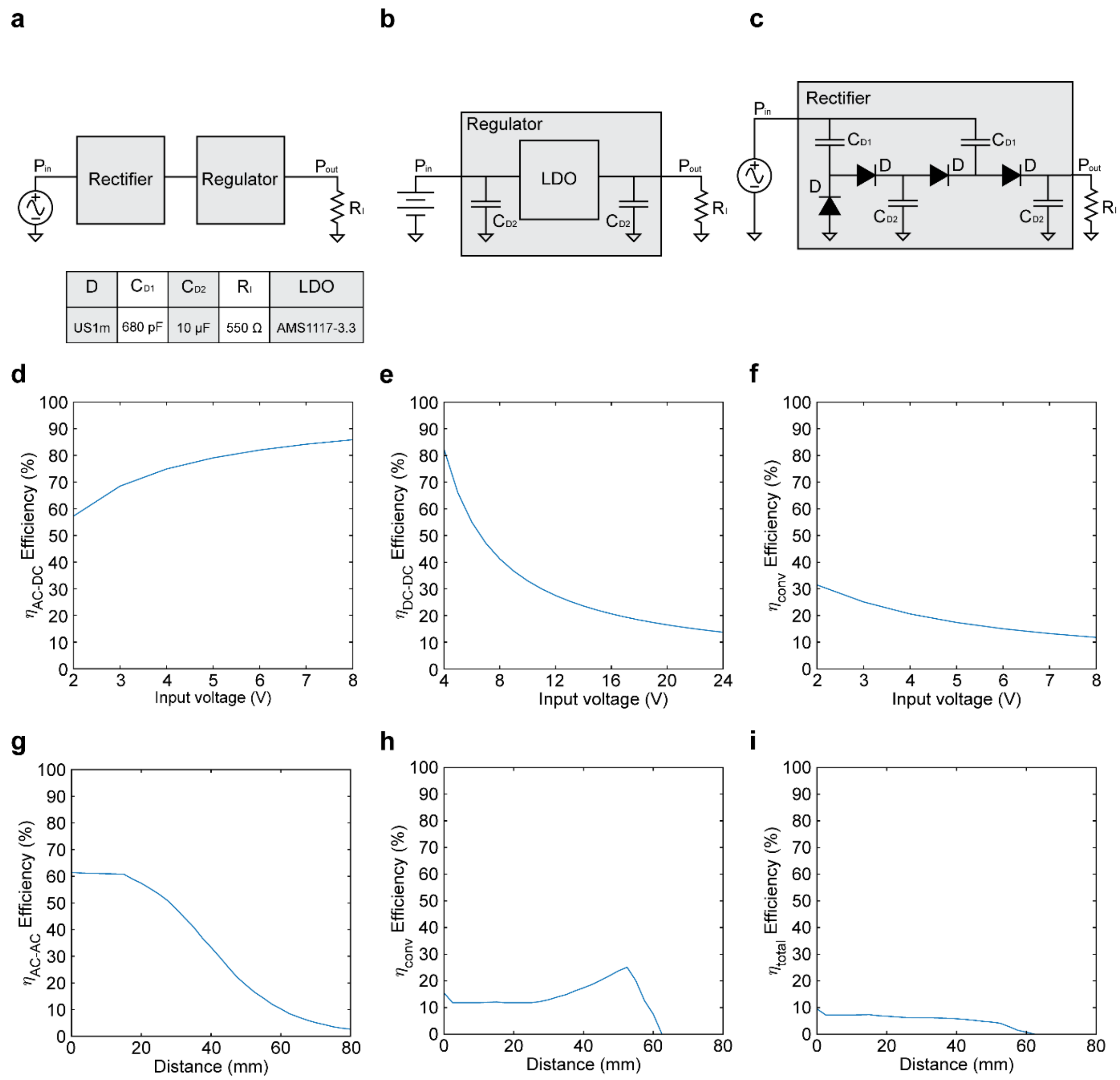

Supplementary Fig. 14 | Efficiency of the wireless power transfer and rectification chain. **a,** Chain of a rectifier and a regulator to convert power from AC to DC. **b,** Circuit schematic to characterize the rectifier efficiency. **c,** Circuit schematic to characterize the LDO regulator efficiency. **d,** Simulated rectifier efficiency (η_{AC-DC}) as a function of input voltage. **e,** Measured regulator efficiency (η_{DC-DC}) as a function of input voltage. **f,** Conversion efficiency (η_{conv}) as a function of input voltage. **g,** Power-transfer efficiency (η_{AC-AC}) as a function of transfer distance between the transmitter and receiver coils. **h,** The conversion efficiency with the input voltage at a corresponding distance. **i,** The measured end-to-end efficiency ($\tilde{\eta}$).

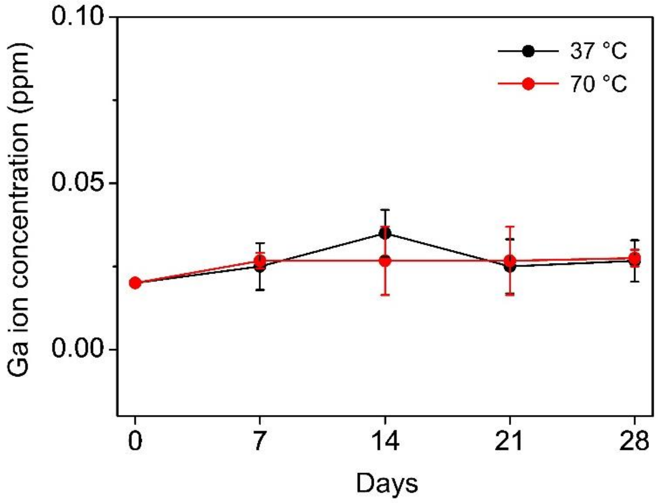

Supplementary Fig. 15 | Chronic stability assessed by ion leaching test. Concentration of gallium (Ga) ions leached from the LM device into phosphate-buffered saline (PBS) over a 28-day immersion period at 37 °C and 70 °C, measured by inductively coupled plasma mass spectrometry (ICP-MS). According to the Arrhenius aging model, 4 weeks at 70 °C is equivalent to approximately 40 weeks of stability at the normal body temperature of 37 °C. The negligible ion concentration (< 0.1 ppm) throughout the test period confirms the effective encapsulation of the LM and supports the device's long-term biocompatibility. Data are presented as mean ± s.d. from measurements on $n = 3$ devices.

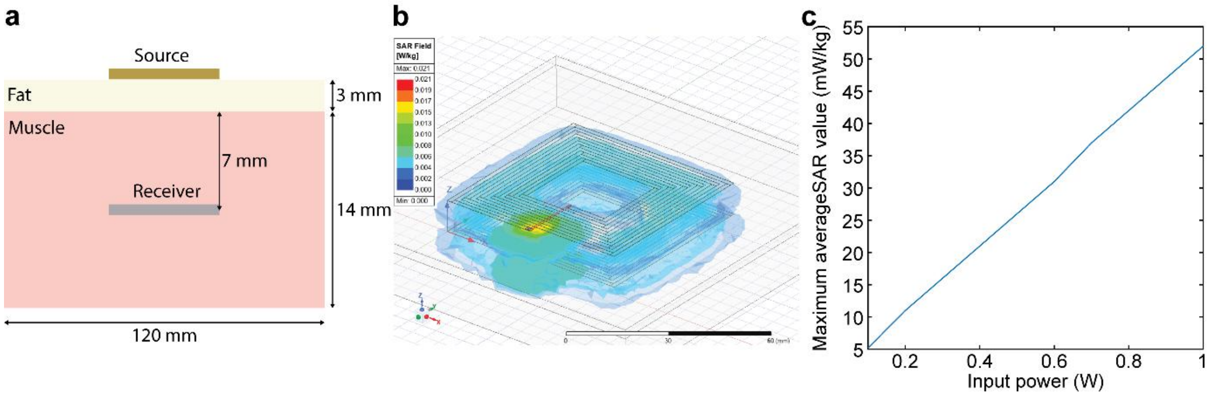

Supplementary Fig. 16 | Simulation of specific absorption rate (SAR). a, Cross-sectional schematic of the tissue model used for electromagnetic simulation. **b,** Simulation of the SAR distribution (W kg^{-1}) with 0.4 W input power for in vivo demonstration. **c,** Maximum averaged SAR value as a function of input power (0.1 – 1 W).

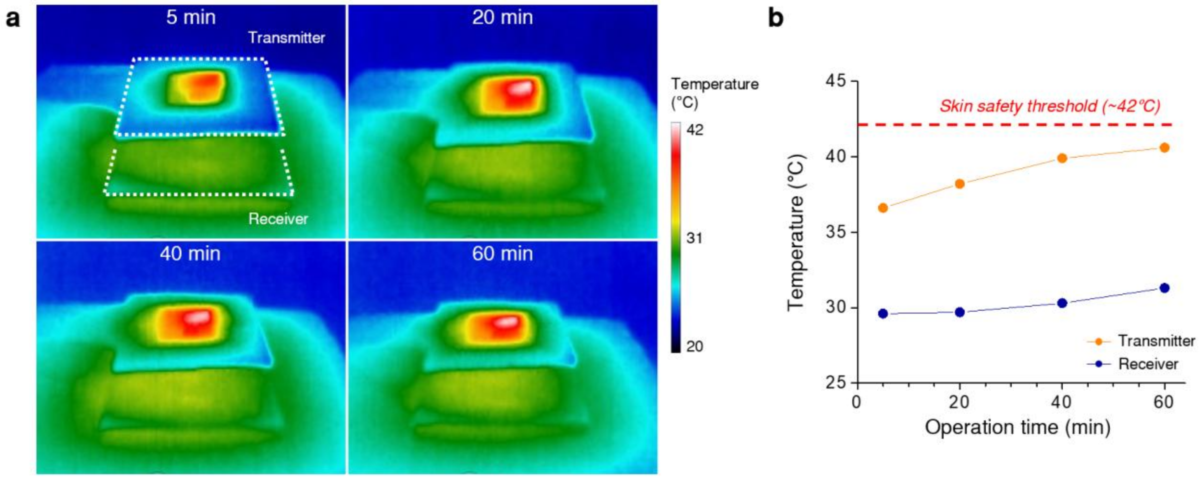

Supplementary Fig. 17 | Thermal safety validation during continuous wireless power transfer. a, Infrared thermography images and **b**, time-dependent temperature profile during 1 hour of continuous operation. To replicate physiological conditions, the receiver was embedded beneath a 20 mm thick porcine tissue layer placed on a 35 °C heating plate, while the transmitter was positioned above the tissue. The maximum temperature at the transmitter surface over 60 minutes of continuous operation reached approximately 40.6 °C. The highest temperature rise was observed at the transmitter circuit region where the feedback coil is located.

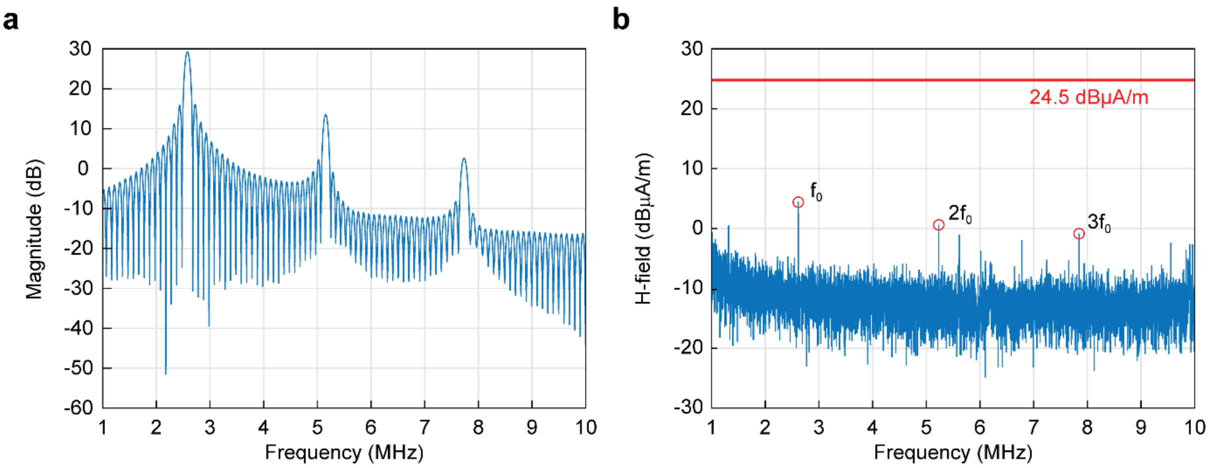

Supplementary Fig. 18 | Electromagnetic interference (EMI) and spectral purity analysis of the self-oscillating system. a, Frequency spectrum of the self-oscillating implementation obtained from a circuit simulation. **b,** Measured magnetic-field emission spectrum using a loop antenna at a 3-m separation. The dashed red line indicates the ETSI EN 300 330 limit at the same distance. Markers indicate the fundamental f_0 and its harmonics.

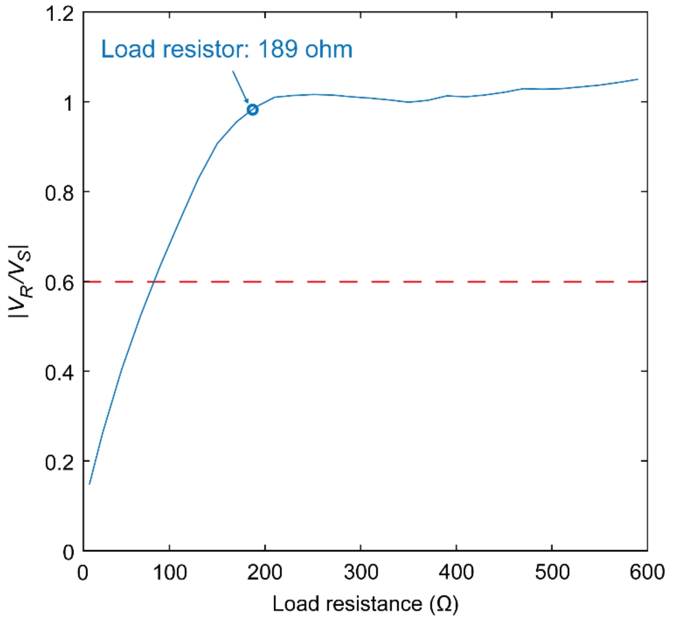

Supplementary Fig. 19 | Characterization of the PT-breaking threshold and operational margin. Simulated transfer efficiency as a function of receiver load resistance. The equivalent load (189 Ω) of the current bioelectronic system is marked on the curve. The dashed red line denotes the minimum voltage ratio required for the functional operation of the circuitry.

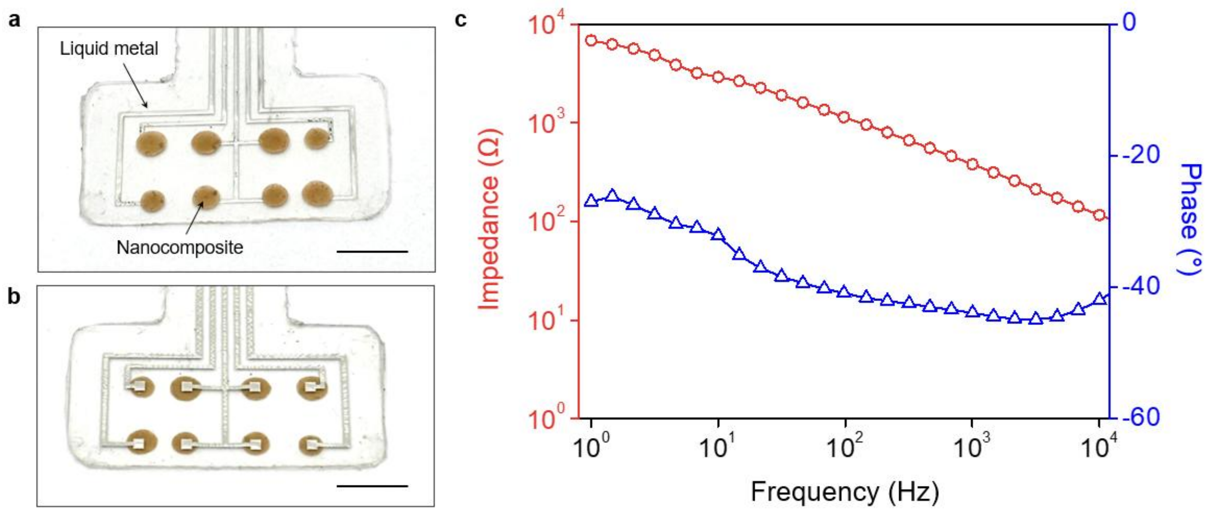

Supplementary Fig. 20 | Nanocomposite-integrated electrodes for cardiac pacing. a,**b**, Optical images of the front **(a)** and back **(b)** sides of the epicardial electrode array. It features low-impedance nanocomposite electrodes for interfacing with tissue, while the back side shows the LM interconnects. Scale bars, 5 mm. **c**, Electrochemical impedance spectroscopy (EIS) measurement of the electrode, showing low impedance (< 3 kΩ at 10 Hz) suitable for effective cardiac stimulation.

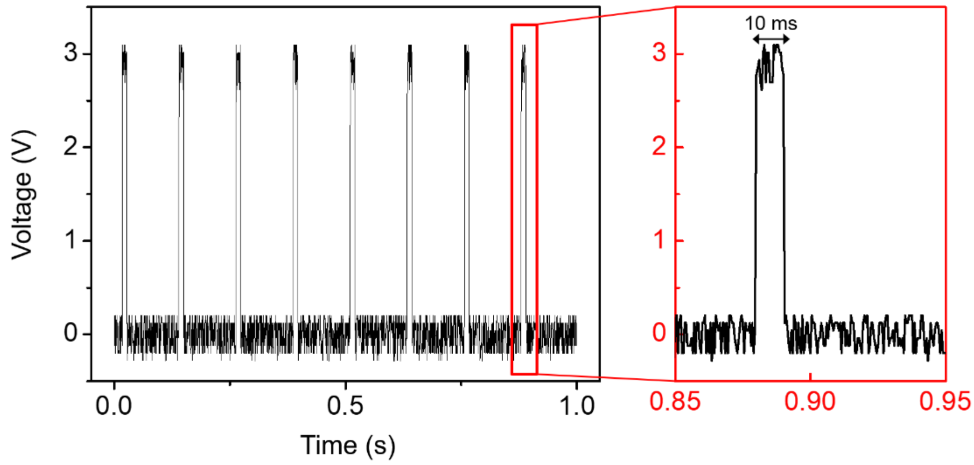

Supplementary Fig. 21 | In vivo pacing signal from the implanted LM device. Recorded voltage output from the electrodes of wirelessly powered LM pacemaker implanted in a rabbit model. The device successfully delivered stable pacing pulses (3 V amplitude, 10 ms pulse width, 8 Hz rate) despite mechanical deformation, confirming its electrical robustness and reliable performance in an *in vivo* environment. The inset shows a magnified view of a single pacing pulse.

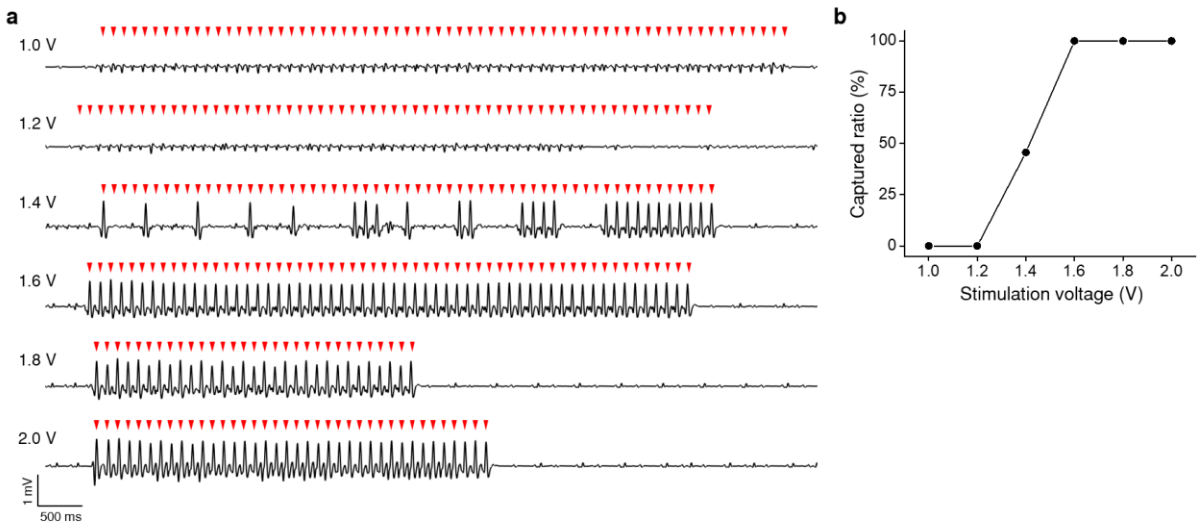

Supplementary Fig. 22 | In vivo pacing performance and threshold determination in a rabbit model. a, ECG traces recorded under varying stimulation voltages (1.0–2.0 V) with fixed parameters (480 bpm, 10 ms pulse width). Consistent cardiac capture, marked by pacing spikes and QRS complexes, is observed at voltages ≥1.6 V. **b**, Pacing capture rate as a function of stimulation voltage.

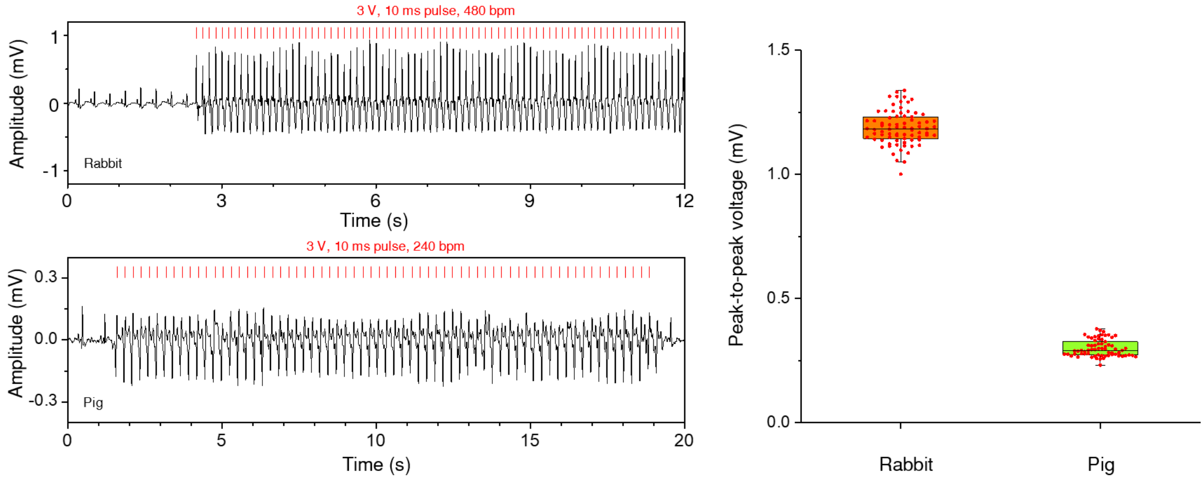

Supplementary Fig. 23 | Stability of in vivo cardiac capture across animal models. Representative ECG traces from Figs. 4f and 5f (left) and peak-to-peak voltage (right) during stimulation. Box plots represent the interquartile range (IQR) with whiskers extending to 1.5×IQR and individual data points overlaid. Mean ± standard deviation values are 1.187 ± 0.068 mV (rabbit) and 0.300 ± 0.034 mV (pig). n = 77 (rabbit), n = 67 (pig) QRS peaks.

Supplementary Table 1 | Performance comparison of different WPT modalities for implantable bioelectronics.

WPT modalities	Capacitive Coupling[7]	Magneto -electric[8,9]	Ultrasound [10,11]	Mid-field[12]	Near-field inductive coupling		
					Standard NIC[13,14]	Adaptive frequency hopping[15,16]	This work (PT-symmetry)
Mechanism	Electric field	Magnetic field	Acoustic wave	Tissue-assisted radiative-to-inductive coupling	Fixed-frequency magnetic resonance	Active tuning	Coupled-mode physics via gain-loss balance
Frequency	10 – 100 MHz	400 kHz	1.8 MHz	1.6 GHz	13 MHz	8 – 12 MHz	2.6 – 4.0 MHz
System-level effiency	Low	Low	Low	Moderate	High		
Maximum depth	Shallow	Deep	Deep	Deep	Mid-range		
Miniaturization	Good	Good	Good	Good	Poor		
Receiving circuit complexity	Low	Low	Moderate	Low	Low	High (needs sensor/comms for feedback)	Low
Advantages	Simple configuration	Alignment tolernace	Very small implants	Good all-around performance	High power implants Simple integration		
Limitations	Shallow depth	No commercial transmitter	Acoustic impedance mismatch	Sensitive to focusing	Poor alignment tolerance	Complexity, latency	Miniaturization (Device >1 cm^2)

Supplementary Table 2 | Performance comparison of PT-symmetric WPT systems.

Study	**Rigid**					**Flexible**	**Stretchable**
	***Nature* (2017)[1]**	***Nat. Electron.* (2020)[3]**	***Phys. Rev. Appl.* (2020)[17]**	***Int. J. Circ. Theor. Appl.* (2023)[18]**	***Commun. Eng.* (2025)[19]**	***Sci. Adv.* (2022)[20]**	**This Work**
Mechanism	Nonlinear PT-symmetry (Op-Amp based)	Switch-mode PT-symmetry (Class-E/D)	High-order PT-symmetry (Three-coil)	Quasi PT-symmetry via gain-loss ratio modulation	Exceptional point pinning via loss control	Heterogeneous & Flippable Neutrals (Five-coil)	Switch-mode PT-symmetry & Strain-insensitive system
Key contribution	Fundamental physics	Circuit efficiency (Switch-mode)	Range extension (Higher-order)	Control methodology	Maximizing transmission efficiency	Robustness under lateral misalignment	Alignment and strain-tolerance, Bio-integration
Operating frequency	2.2-2.6 MHz, f_0 ~2.50 MHz	2.0-2.4 MHz, f_0 ~2.37 MHz	~86.8 kHz	273-303 kHz	~85 kHz	12-15 MHz, f_0 ~15 MHz	2.6-4.0 MHz, f_0 ~2.64 MHz
Magnetic coupler type	Copper coil, D ~58 cm	Copper coil, D ~58 cm	Copper coil, D ~60 cm	Copper coil, D ~40 cm	Ferrite-enhanced Litz wire coil, D ~40 cm	Copper-Polyimide, 3.0 cm × 1.8 cm	Liquid metal-Elastomer, 6.0 cm × 6.0 cm
Transfer distance	~70 cm	~70 cm	~80 cm	~40 cm	~30 cm	~1.5 cm	~4 cm
Transfer efficiency	84% at 70 cm distance	92% at 65 cm distance	80% at 80 cm distance	70% at 20 cm distance	98% transmission efficiency at 20 cm distance	35% at 1.2 cm distance and 3.0 cm lateral displacement	50% at 3 cm distance and 30% strain
System integration	Benchtop circuit	Benchtop circuit	Benchtop circuit	Benchtop circuit	Benchtop circuit	Benchtop circuit	Wearable Tx + Implantable Rx
Load at receiver	Linear (a resistor or a light bulb)	Linear (a resistor)	Linear (a resistor)	Linear (a resistor)	Linear (a resistor)	Linear (a resistor)	Nonlinear (a rectifier, a regulator, a microcontrol unit)
Bio applicability	N/A	N/A	N/A	N/A	N/A	Ex vivo (Porcine tissue)	In vivo (Rabbit, Porcine)

Supplementary Table 3 | Performance comparison with representative wireless bioelectronics that have been reported in recent years.

Material	Frequency	Transmitter	Receiver	Stretchability	Efficiency	Ref.
			Implantable applications			
EGaIn, SEBS, SBS, Ecoflex	**2.64 MHz**	**6 cm × 6 cm**	**6 cm × 6 cm**	**220%**	**Transfer efficiency = 94.0% (no strain), 91.5% (30% strain) at 1 cm distance; 67.4% (no strain), 50.5% (30% strain) at 3 cm distance**	**This work**
AgNW, PU	50 MHz	D = 5.5 cm	D = 3 cm	100%	PTE = 76.0% (no strain), 74.8% (50% strain)	21
Galinstan, Ecoflex	12 MHz	D = 1.5 cm	D = 5 cm	200%	Q = 29 at 13.5 MHz (no strain), 22 at 10.2 MHz (200% strain)	22
EGaIn, PDMS	220 kHz	Around the body	Stent tube (D = 2 cm)	140%	V_{OC} = 10.66 V (no strain), 5.46 V (compressed to 70%)	23
Mg, Mo, PLGA	5 MHz	D = 8 cm	D = 1.6 cm	Flexible	PTE = 0.9% at 0 mm distance, 0.5% at 20mm distance	24
Tungsten-coated Mg, PLGA	13.5 MHz	D = 2.5 cm	D = 2.5 cm	Flexible	PTE = 22.5% at 5 mm distance, 7.5% at 12.5 mm distance	25
Cu, Au, PI, SEBS	1 MHz	R = 3 cm, hexagon	12 mm × 7.5 mm	Flexible	PTE = 3.5% at 2 cm distance	26
Mo, PU	14.8 MHz	D = 6 cm	D = 2.4 cm	Flexible	V_{OC} = 16 V at 2 mm distance, 2V at 11 mm distance	27
Au, Cu, PI, Parylene	13.56 MHz	56 cm × 16 cm cage	3.5 cm × 2.5 cm	Flexible	Received power = 120 mW (6% of input)	28
Cu, PI	6.78 MHz	D = 20 cm, H = 13 cm cage	2.3 cm × 1.5 cm	Flexible	Received power = 30 mW (3.75% of input)	29
Cu, PI	13.56 MHz	22 cm × 22 cm cage	D = 1.67 mm	Flexible	Received power = 32 mW (0.4% of input)	30

Cu, PI, Parylene	13.56 MHz	20 cm × 35 cm × 35 cm	D = 1 cm	Flexible	Received power = 14.61 mW (1.4% of input)	31
Cu, Pt , PI, Parylene	13.56 MHz	14 cm × 25 cm cage	D = 11.2 mm	Flexible	Received power = 8.4 - 14 mW	32
Cu, PI	13.56 MHz	28 cm × 22 cm cage	0.5 mm × 0.2 mm, dual layer	Flexible	Received power = 18 mW (0.6% of input)	33
Cu, PI	13.56 MHz	45 cm × 12 cm cage	26 mm x 16 mm	Flexible	NA	34
Cu, PI	13.56 MHz	NA	D = 1 cm	Flexible	Received power = 15mW	35
Wearable applications						
Ag flake, $BaTiO_3$-Ecoflex composite	13.56 MHz	D = 5.5 cm	2 cm × 3 cm	380%	PTE = 51% (no strain), 52% (30% strain) at 3 mm distance; 20% (no strain), 18% (30% strain) at 30 mm distance	36
Ag nanofiber, PDMS	20 MHz	D = 4 cm	D = 4 cm	100%	PTE = 37% (no strain), 27% (50% strain)	37
Ag foil, CNT/ AgNW ink, PU	145 kHz	D = 12 cm	2 cm × 2.5 cm	200%	Received power = 11.71 W at 200% strain	38
Galinstan, PDMS	13.5 MHz	8.5 cm × 6.2 cm	D = 2 cm	50%	Q = 4.3 at 13.5 MHz (0% strain), 3.9 at 12.8 MHz (30% strain)	39

Q: quality factor; V_{OC}: open circuit voltage; PTE: power transfer efficiency; AgNW: silver nanowire; PU: polyurethane; PI: polyimide; PLGA: poly(lactic-co-glycolic acid); CNT: carbon nanotube.

Supplementary Video 1. Variation-tolerant wireless power transfer system using liquid metal electronics and PT-symmetric resonance.

Supplementary Video 2. Fully untethered cardiac pacing by wearable-to-implant wireless power transfer system demonstrated in an in vivo porcine model. The illustration titled “Fully untethered cardiac pacing system” in this video was created with BioRender.com.

Reference

1. Assawaworrarit, S., Yu, X. & Fan, S. Robust wireless power transfer using a nonlinear parity–time-symmetric circuit. *Nature* **546**, 387–390 (2017).
2. Wang, H., Assawaworrarit, S. & Fan, S. Dynamics for encircling an exceptional point in a nonlinear non-Hermitian system. *Opt. Lett.* **44**, 638–641 (2019).
3. Assawaworrarit, S. & Fan, S. Robust and efficient wireless power transfer using a switch-mode implementation of a nonlinear parity–time symmetric circuit. *Nat. Electron.* **3**, 273–279 (2020).
4. Ahlbom, A. et al. Guidelines for limiting exposure to time-varying electric, magnetic, and electromagnetic fields (up to 300 GHz). Health Physics 74 (4), 494-521 (1998).
5. Specification for Radio Disturbance and Immunity Measuring Apparatus and Methods - Part 1-4: Radio Disturbance and Immunity Measuring Apparatus - Antennas and Test Sites for Radiated Disturbance Measurements, CISPR 16-1-4 ed.4.0 (2023).
6. Short Range Devices (SRD); Radio equipment in the frequency range 9 kHz to 25 MHz and inductive loop systems in the frequency range 9 kHz to 30 MHz; Harmonised Standard covering the essential requirements of article 3.2 of Directive 2014/53/EU, ETSI EN 300 330 V2.1.1 (2017).
7. Kurs, A. *et al.* Wireless power transfer via strongly coupled magnetic resonances. *Science* **317**, 83–86 (2007).
8. Chen, J. C., *et al.* Self-rectifying magnetoelectric metamaterials for remote neural stimulation and motor function restoration. *Nat. Mater.* **23**, 139–146 (2024).
9. Chen, J. C. *et al.* Endocisternal interfaces for minimally invasive neural stimulation and recording of the brain and spinal cord. *Nat. Biomed. Eng* **9**, 896–904 (2025).

10. Zeng, Y. *et al.* A programmable and self-adaptive ultrasonic wireless implant for personalized chronic pain management. *Nat. Electron.* **8**, 437–449 (2025).

11. Hinchet, R. *et al.*Transcutaneous ultrasound energy harvesting using capacitive triboelectric technology. *Science* **365**, 491–494 (2019).

12. Ho, J. S. *et al.* Midfield wireless powering for implantable systems. *Proc. IEEE* **101**, 1369–1378 (2013).

13. Jung, T. *et al.* A wireless subdural-contained brain–computer interface with 65,536 electrodes and 1,024 channels. *Nat. Electron.* **8**, 1272–1288 (2025).

14. Yin, D. *et al.* A battery-free nanofluidic intracellular delivery patch for internal organs. *Nature* **642**, 1051–1061 (2025).

15. Sample, A. P. *et al.* Analysis, experimental results, and range adaptation of magnetically coupled resonators for wireless power transfer. *IEEE Trans. Ind. Electron.* **58**, 544–554 (2011).

16. Lim, Y. *et al.* An adaptive impedance-matching network based on a novel capacitor matrix for wireless power transfer. *IEEE Trans. Power Electron.* **29**, 4403–4413 (2014).

17. Zeng, C. *et al.* High-order parity-time symmetric model for stable three-coil wireless power transfer. *Phys. Rev. Applied* **13**, 034054 (2020).

18. Hu, W.-K. *et al.* Maximizing wireless power transfer efficiency at exceptional points. *Commun. Eng.* **4**, 105 (2025).

19. Li, J. *et al.* A wireless power transfer system based on quasi-parity–time symmetry with gain–loss ratio modulation. *Int. J. Circ. Theor. Appl.* **51**, 1039–1056 (2023).

20. Kim, H. *et al.* Wide-range robust wireless power transfer using heterogeneously coupled and flippable neutrals in parity-time symmetry. *Sci. Adv.* **8**, 1–11 (2022).

21. Xu, Y. *et al.* Phase-separated porous nanocomposite with ultralow percolation threshold for wireless bioelectronics. *Nat. Nanotechnol.* **19**, 1158–1167 (2024).

22. Yamagishi, K., Zhou, W., Ching, T., Huang, S. Y. & Hashimoto, M. Ultra-Deformable and Tissue-Adhesive Liquid Metal Antennas with High Wireless Powering Efficiency. *Adv. Mater.* **33**, 1–15 (2021).

23. Zhang, C. *et al.* Wirelessly powered deformable electronic stent for noninvasive electrical stimulation of lower esophageal sphincter. *Sci. Adv.* **9**, 1–11 (2023).

24. Koo, J. *et al.* Wireless bioresorbable electronic system enables sustained nonpharmacological neuroregenerative therapy. *Nat. Med.* **24**, 1830–1836 (2018).

25. Choi, Y. S. *et al.* Fully implantable and bioresorbable cardiac pacemakers without leads or batteries. *Nat. Biotechnol.* **39**, 1228–1238 (2021).

26. Wang, S. *et al.* A self-assembled implantable microtubular pacemaker for wireless cardiac electrotherapy. *Sci. Adv.* **9**, 1–10 (2023).

27. Choi, Y. S. *et al.* Stretchable, dynamic covalent polymers for soft, long-lived bioresorbable electronic stimulators designed to facilitate neuromuscular regeneration. *Nat. Commun.* **11**, 5990 (2020).

28. Burton, A. *et al.* Fully implanted battery-free high power platform for chronic spinal and muscular functional electrical stimulation. *Nat. Commun.* **14**, 7887 (2023).

29. Lee, J. H. *et al.* Wireless, Fully Implantable and Expandable Electronic System for Bidirectional Electrical Neuromodulation of the Urinary Bladder. *ACS Nano* **17**, 8511–8520 (2023).

30. Ausra, J. *et al.* Wireless, fully implantable cardiac stimulation and recording with on-device computation for closed-loop pacing and defibrillation. *Sci. Adv.* **8**, 1–15 (2022).

31. Ausra, J. *et al.* Wireless battery free fully implantable multimodal recording and neuromodulation tools for songbirds. *Nat. Commun.* **12**, 1968 (2021).

32. Gutruf, P. *et al.* Wireless, battery-free, fully implantable multimodal and multisite pacemakers for applications in small animal models. *Nat. Commun.* **10**, 5742 (2019).

33. Burton, A. *et al.* Wireless, battery-free, and fully implantable electrical neurostimulation in freely moving rodents. *Microsystems Nanoeng.* **7**, 62 (2021).

34. Cai, L. *et al.* Osseosurface electronics—thin, wireless, battery-free and multimodal musculoskeletal biointerfaces. *Nat. Commun.* **12**, 6707 (2021).

35. Zhang, Y. *et al.* Battery-free, fully implantable optofluidic cuff system for wireless optogenetic and pharmacological neuromodulation of peripheral nerves. *Sci. Adv.* **5**, 1–11 (2019).

36. Kim, S. H. *et al.* Strain-invariant stretchable radio-frequency electronics. *Nature* **629**, 1047–1054 (2024).

37. Zhang, Y. *et al.* High precision epidermal radio frequency antenna via nanofiber network for wireless stretchable multifunction electronics. *Nat. Commun.* **11**, 5629 (2020).

38. Wang, Y. *et al.* Deformation-tolerant, wireless-charging microbatteries for seamlessly integrated omnidirectional stretchable electronics. *Sci. Adv.* **11**, 1–11 (2025).

39. Jeong, Y. R. *et al.* A skin-attachable, stretchable integrated system based on liquid GaInSn for wireless human motion monitoring with multi-site sensing capabilities. *NPG Asia Mater.* **9**, e443–e443 (2017).